ACS APPLIED ENERGY MATERIALS

Subscriber access provided by Karolinska Institutet, University Library

Article

NH- and CH- substituted Ureas as self-assembly directing motifs for facile synthesis and electrocapacitive applications of advanced WO3-x 1D nanorods

Akshay Vinod Salkar, Ravi X Fernandes, Sheshanath V Bhosale, and Pranay Morajkar

ACS Appl. Energy Mater., **Just Accepted Manuscript** • DOI: 10.1021/acsaem.9b01704 • Publication Date (Web): 20 Nov 2019

Downloaded from pubs.acs.org on November 20, 2019

Just Accepted

"Just Accepted" manuscripts have been peer-reviewed and accepted for publication. They are posted online prior to technical editing, formatting for publication and author proofing. The American Chemical Society provides "Just Accepted" as a service to the research community to expedite the dissemination of scientific material as soon as possible after acceptance. "Just Accepted" manuscripts appear in full in PDF format accompanied by an HTML abstract. "Just Accepted" manuscripts have been fully peer reviewed, but should not be considered the official version of record. They are citable by the Digital Object Identifier (DOI®). "Just Accepted" is an optional service offered to authors. Therefore, the "Just Accepted" Web site may not include all articles that will be published in the journal. After a manuscript is technically edited and formatted, it will be removed from the "Just Accepted" Web site and published as an ASAP article. Note that technical editing may introduce minor changes to the manuscript text and/or graphics which could affect content, and all legal disclaimers and ethical guidelines that apply to the journal pertain. ACS cannot be held responsible for errors or consequences arising from the use of information contained in these "Just Accepted" manuscripts.

is published by the American Chemical Society. 1155 Sixteenth Street N.W., Washington, DC 20036

Published by American Chemical Society. Copyright © American Chemical Society. However, no copyright claim is made to original U.S. Government works, or works produced by employees of any Commonwealth realm Crown government in the course of their duties.

NH- and CH- substituted Ureas as self-assembly directing motifs for facile synthesis and electrocapacitive applications of advanced WO_{3-x} 1D nanorods

Akshay V. Salkar[a], Ravi X. Fernandes[b], Sheshanath V. Bhosale[a], Pranay P. Morajkar[a,c,*]

[a] *School of Chemical Sciences, Goa University, Taleigao Plateau, 403206, Goa, India.*

[b] *Thermophysical Quantities, Physikalisch-Technische Bundesanstalt, 38116 Braunschweig, Germany.*

[c] *Department of Chemical Engineering, Khalifa University of Science & Technology, 2533, Abu Dhabi, U.A.E.*

*Corresponding Authors*E-mail: pranay@unigoa.ac.in*

Dedicated to Prof. Julio B. Fernandes on the occasion of his 66th birthday

ABSTRACT

Designing a solid state crystal architecture at nanoscale using soft chemistry approach, is the key step towards their scalable synthesis for sustainable application in electrochemical charge storage devices. We investigate the application of NH- and CH- substituted ureas namely, carbohydrazide, semicarbazide, N-methylurea and tetramethylurea as design elements/motifs in the tailored synthesis of WO_{3-x} nanostructures via direct calcination of tungstic acid-substituted urea hybrid gels. The SEM, HRTEM, SAED, XRD, XPS and TG-DTA studies reveal that, NH-substitution in urea induces a profound growth of WO_{3-x} 1D nanorods, preferentially growing along the (002) plane with enhancement in the percentage of oxygen vacancies. On the contrary, with the increase in CH- substitution in urea, the tendency to form 1D nanorods via self- assembly process decreases, possibly due to an increase in the steric effect of the methyl groups. We further demonstrate the corresponding effect of morphological and chemical changes in WO_{3-x} nanostructure on their improved electrified interfacial processes via H^+ intercalation using cyclic voltammetry,

galvanostatic charge – discharge, electrochemical impedance spectroscopy tests and chronoamperometric studies. Our findings reveal that the enhancement in WO_{3-x} nanorod growth, W^{5+}/W^{6+} redox surface states and abundance of (002) surface plane due to NH-substitution in urea, plays a crucial role in facilitating the diffusion process of H^+/e^- in and out of the WO_{3-x} matrix. An area specific capacitance of 132 mF cm^{-2} at the current density of 1 mA cm^{-2} with excellent capacitance retention is reported. Moreover, significant improvement in the charge discharge times were observed, highest being the one for WO_{3-x} nanorods obtained using carbohydrazide, demonstrating its potential for possible application in designing 1D nanomaterials for energy storage systems.

KEYWORDS: WO_{3-x} nanorods, NH- and CH- substituted urea, oxygen vacancies, XPS, diffusion coefficient, charge-discharge, electrocapacitance

1. INTRODUCTION

Design and tailored synthesis of nanostructured materials with morphological control is an important prerequisite towards unraveling the full potential of nanomaterials for their varied applications.[1,2] Nanostructured tungsten oxide has attracted vast attention in recent decades due to its effective use in applications ranging from capacitors,[3,4] electrochromics,[5,6] optoelectronics,[7,8] gas-sensing,[9,10] photoelectrocatalytic water-splitting[11,12] and gas-solid interphase catalysis.[13,14] Being a material with such multi-domain applications, tailoring a desirable property demands stringent control over the phase, morphology and chemical composition of WO_3 at the nanoscale level.[15,16] This is challenging because, WO_3 exists in a number of phases and a thorough understanding of the structure-property relationships and reaction mechanism becomes crucial for its tailored synthesis and application. WO_3 nanostructures, especially nanorods have been synthesized till date using various techniques such as chemical vapor deposition, anodic oxidation, laser ablation, hydro/solvothermal treatments etc.[17–21] But the biggest constraint is the requirement of expensive instrumental techniques, the associated safety hazards of very high pressure (180 bar) which limit their safe and cost effective, scalable industrial production and device scale application. Thus, it becomes meaningful to device a simple and tunable synthetic route for synthesis of WO_3 nanorods.

In recent times, WO_{3-x} as an efficient, redox nanomaterial, produced by intentionally inducing partial oxygen deficiencies on the WO_3 surface, has gained a lot of attention.[22–25] The presence of oxygen deficiencies and redox oxidation states (W^{5+}/W^{6+}) have been reported to improve the electrochemical performance by enhancing the electrical conductivity and providing more active sites, greatly facilitating the charge transfer between WO_{3-x} and the electrolyte.[25–27] The applications of WO_{3-x} are therefore vast and ranges from capacitors, Li ion/ Li air batteries, water

splitting etc.[23,28,29] Many post synthesis WO_3 reduction methods using H_2 or NH_3 etc. have also been utilized to synthesize WO_{3-x} till date.[30,31] However, these post synthesis reduction treatments add on to the cost and time of material production and hence, newer and improved strategies involving controlled in situ partial reduction for the synthesis of WO_{3-x} nanostructures are constantly being investigated.

Multifunctional organic molecules which can act as both structure directing motifs as well as energy rich fuels in combustion synthesis, play a vital role in tailoring the surface morphologies of a variety of transition metal nanostructures.[32–34] Urea is one such organic compound that has the ability to form persistent hydrogen-bonded chains in a variety of environments. This characteristic hydrogen bonding feature has made urea an attractive candidate for supramolecular chemistry.[35] The nature of the substituents on the nitrogen atom in urea has a direct effect on its hydrogen bonding attributes, thus making it a robust and tunable building block.[36] A wide variety of building blocks can be produced by substitution in urea which can be applied as assembly directing motifs towards construction of nanostructured materials.[37,38] Urea has a unique feature wherein, it can act both as a hydrogen donor through its NH protons as well as an acceptor through the lone pair of the C=O group. Elucidating this mechanism becomes crucial, since the good complementarity between the two groups can result in self-association into robust one-dimensional hydrogen bonded chains, which can be further applied to produce nanostructured materials based on rod like, tubular or columnar architectures.[36,39] In comparison to urea, substituted ureas have been far less explored for the rational design of nanomaterials, despite the fact that they can also form relatively robust hydrogen-bonded motifs. Understanding the fundamental chemistry of urea becomes crucial at this point to identify what makes urea a nanorod growth promoter. In our previous work[40] we demonstrated two critical parameters i.e. 1) the mono-protonation of urea at

the carbonyl oxygen which results in the formation of an iminium cation (-C=NH_2^+) which facilitates the kinetics of one dimensional growth and 2) the exothermic decomposition of urea satisfies the thermodynamic requirements for transforming particles of WO_3 into stable solid state 1D nanorods. However, since urea is a sluggish fuel there exists a significant scope to improve upon its exothermic decomposition efficiency. Several research groups have utilized hydrazine as an alternative fuel to urea in combustion synthesis due to its ability to undergo rapid exothermic decomposition.[33,41] However, the lack of O-protonation center, inability to act as assembly directing motif and excessive particle sintering induced by explosive nature of its exothermic decomposition has severely restricted its use in designing nanostructured materials. On the contrary, NH- substituted ureas such as semicarbazide and carbohydrazide which are traditionally prepared in laboratory by combining hydrazine and urea, could prove to be the perfect balance of nanostructure directing ability with improved exothermicity and can further promote the one dimensional growth of WO_3 nanostructures. On the contrary, if the NH- substitution is replaced by CH- substitution in urea, this could have detrimental effects on its nanostructuring ability to direct the growth of nanorods. More importantly, altering the degree of NH- substitution in urea, its decomposition pattern in the metal-precursor hybrid gels can be tuned to achieve controlled in situ reduction of WO_3 surface to synthesize advanced 1D WO_{3-x} nanostructures. This in turn would have a direct effect on its electrochemical performance and charge-discharge characteristics as discussed earlier. However, the role of NH- and CH- substituted ureas as assembly directing motifs for synthesizing advanced WO_{3-x} nanostructures is not well understood and its influence on electro capacitive characteristics of WO_{3-x} has never been investigated till date to the best of our knowledge. Therefore, in the present work, we put the above hypothesis to test by utilizing NH- and CH- substituted, O-protonated ureas in a dual role, i.e. to act as a fuel, as well as, a cost

effective nanostructure directing motif, for synthesizing 1D WO_{3-x} nanorods. The resulting effect of NH- and CH- substitution on the decomposition pattern of metal precursor, WO_{3-x} nanorod morphology, percentage distribution of redox states and corresponding influence on electrocapacitive performance have been investigated. The findings of this study reveal that, the NH- substituted urea can act as superior assembly directing motifs, altering the surface nanostructure and chemical composition in a way that facilitates the diffusion process of electrons in and out of the WO_{3-x} matrix, rendering improved electro capacitive performance. The significant improvement in the charge-discharge times measured for WO_{3-x} nanorods synthesized using carbohydrazide as nanostructure directing motif, demonstrates its promising potential in designing 1D nanomaterials for application in energy storage systems. These interesting results are discussed in detail in the subsequent sections.

2. EXPERIMENTAL SECTION

2.1 Materials: Sodium tungstate dihydrate ($Na_2WO_4.2H_2O$, 99%), Urea (CH_4N_2O, 99%), were purchased from Spectrochem Pvt. Ltd. Hydrochloric acid (HCl) and Sulphuric acid (H_2SO_4) were purchased from Fisher Scientific, India. N-Methylurea ($C_2H_6N_2O$, 97%), Tetramethylurea ($C_5H_{12}N_2O$) and Nafion 117 solution were acquired from Sigma-Aldrich and Carbohydrazide (CH_6N_4O, 97%) along with Semicarbazide hydrochloride ($CH_5N_3O.HCl$, 99%) were purchased from Alfa Aesar. All the chemicals were used without further purification.

2.2 Synthesis of nanostructured WO_{3-x}: In a typical sample preparation procedure, 1.42 g of sodium tungstate dihydrate was added to 10 mL of deionized water with stirring for 10 minutes to

form a clear solution. 30 mL of 2 M HCl was added drop wise to this solution in order to form a colloidal tungstic acid gel. This gel was then washed to remove Na^+ and Cl^- ions by centrifugal filtration. This was termed as solution **A**. 4.76 g of NH- or CH- substituted ureas as desired were dissolved in 20 mL of deionized water to form solution **B**. Solution B was added dropwise to solution A under constant stirring, in order to form the colloidal tungstic acid-substituted urea hybrid gel precursor. The pH of the solution was adjusted to 2 by using HCl. The hybrid gel was digested on a water bath at 90 °C for 3 h. The obtained semi solid precipitate was calcined in air at 550 °C for 2 h in a muffle furnace. The WO_{3-x} obtained after calcination were characterized for phase purity, composition and morphology in comparison to WO_{3-x} nanorods synthesized in a similar manner using urea in our previous work.[40]

2.3 Material Characterization: The surface functionalities of the WO_{3-x} nanorods were evaluated using IR spectroscopy, Shimadzu IR- Pristige-21. Phase and structure of synthesized WO_{3-x} (after calcination) was investigated by powder X-ray diffraction using PXRD, Philips PW-1840 with Cu K alpha (k=0.154 nm) and nickel as filter over the 2θ range of 10-80°. The morphology of the WO_{3-x} nanorods were determined by using scanning electron microscopy using SEM, Carl-Zeiss JSM-5800LV coupled with Ametek edx PV6500 and further investigated using transmission electron microscope (Tecnai TEM 200 kV) by mounting the sample on a Lacey carbon coated 400 mesh Cu TEM grid. XPS analysis were carried out using a Kratos Axis Supra DLD spectrometer equipped with a monochromatic Al Kα X-ray source (hν = 1486.6 eV) operating at 150 W, a multi-channel plate and delay line detector under a vacuum of ~10^{-9} mbar. The thermal decomposition behavior of the synthesized tungstic acid-substituted urea hybrid gels were analyzed using thermogravimetric analyzer (NETZSCH STA 409PC-LUXX), with heating rate fixed to 5 °C min^{-1}. The BET surface areas were measured using Autosorb IQ QUA 211011.

2.4 Electrochemical evaluation: The electrochemical performance was evaluated using a standard three electrode system with a CHI 660 E series potentiostat. Glassy carbon fabricated with a WO_{3-x} film, Ag/AgCl $_{(aq\ KCl)}$ and Pt wire were used as working, reference and counter electrodes, respectively. Typical CV measurements were performed in a potential range of −0.2 to 1.0 V at a scan rate of 50 mV s^{-1} in 0.5 M sulphuric acid solution. The galvanostatic charge/discharge curves were recorded on a WO_{3-x} modified glassy carbon electrodes at various current densities of 1 – 3 mA cm^{-2} in a potential range of 0.0 to - 0.5 V in 0.5 M sulphuric acid solution. The Electrochemical impedance spectroscopy (EIS) tests were conducted at a frequency range of 1 Hz to 1 MHz with a potential amplitude of 10 mV. The WO_{3-x} electrodes were fabricated using a modified procedure from the literature,[42] wherein the film was fabricated by dispersing a 20 mg of the catalyst (WO_{3-x}) in a mixture of 1000 µl deionized water and 10 µl 5 wt% Nafion 117 solution. A known quantity of the dispersion was mounted on the glassy carbon electrode. The excess solvent was slowly evaporated in an oven at 55 °C. 5 µl of 5 wt % Nafion was coated onto the pre-dried electrode as a binder and the electrode was dried once again in an oven at 55 °C.

3. RESULTS AND DISCUSSION

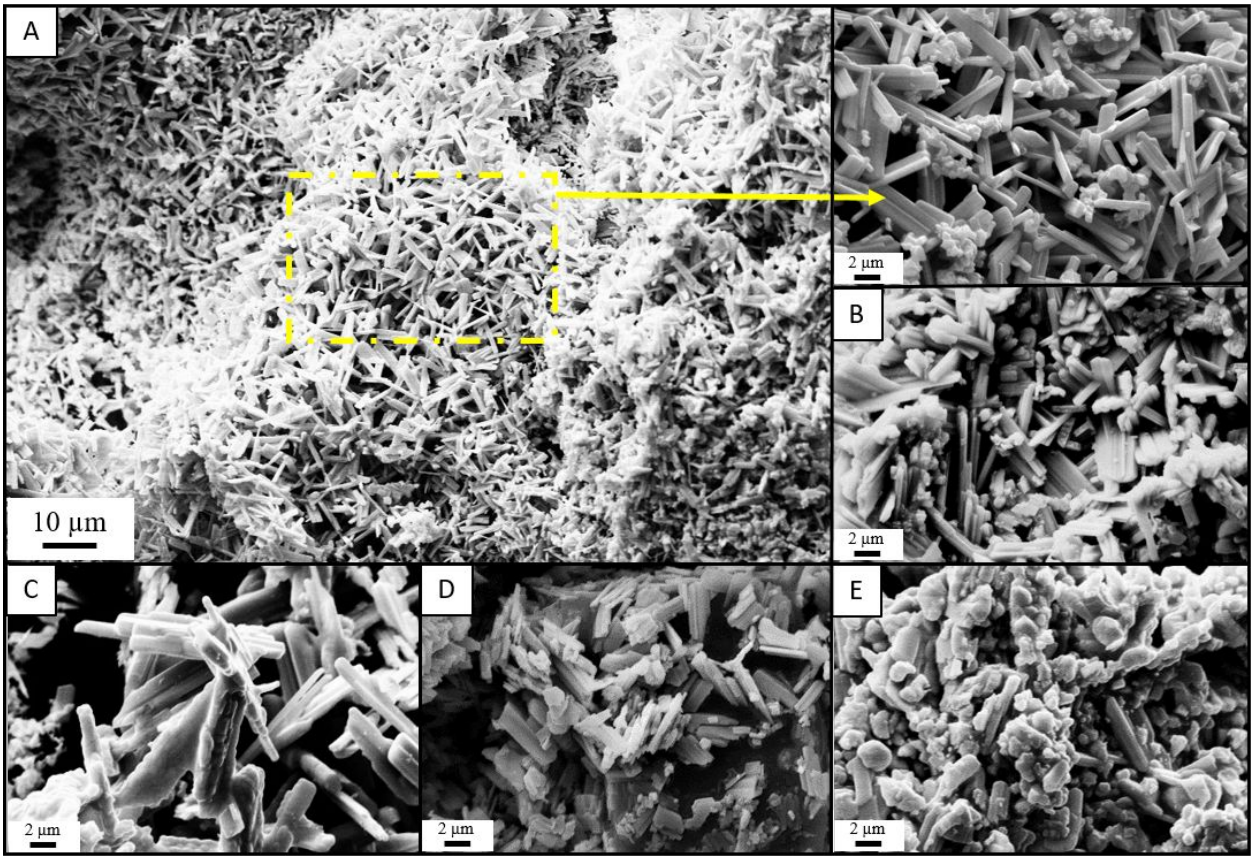

Figure 1: SEM images of WO_{3-x} synthesized by calcining tungstic acid gels with (A) carbohydrazide (B) urea[40] *(adapted from ref. 40 with permission from The Royal Society of Chemistry)* (C) semicarbazide (D) N-methyl urea and (E) tetramethylurea

Fig. 1 A-E presents the SEM images of synthesized WO_{3-x} using carbohydrazide, urea, semicarbazide, N-methyl urea and tetramethylurea, labelled as WC, WU, WSC, WN and WT respectively. It is evident from the SEM results that calcination of tungstic acid gels with carbohydrazide and urea produces fully grown nanorods of varying diameter in the range of 100-200 nm and 2-7 µm in length respectively. In comparison to the WU, WC exhibited a profound growth and homogeneous distribution of nanorods. Further moving in the direction of NH-substitution, the WSC yields relatively much poor nanorod characteristics as evident from Fig. 1 C. From Fig. 1 D and E it is observed that CH- substituted ureas such as N-methylurea lead to only partial/incomplete growth of rod like morphologies, while tetramethylurea largely produced

mixed, rod- particle aggregates with incompletely formed/ deformed rod like structures visible in the mixture.

To investigate the detailed morphological and structural characteristics, the synthesized WO_{3-x} samples were subjected to HRTEM and SAED analysis. The typical representative results, one containing fully grown nanorods (WC) and the second with a mixture of rod like and particle agglomerates (WT) are presented in Fig. 2. Fig. 2A revealed that, the average diameter of ~ 115 nm for the nanorods with an average length of ~ 500 nm, measured through TEM analysis is in good agreement with results of SEM analysis. The HRTEM images of fully formed nanorod morphologies shown in Fig. 2B reveals the lattice fringes with a d-spacing of 0.382 nm, which matches with the (002) plane of monoclinic WO_{3-x} in agreement with the literature reports.[43,44] The selected-area electron diffraction (SAED) pattern (Fig. 2C) also reveals the (002) plane which can be indexed to a monoclinic phase of WO_3 (JCPDS No. 43-1035) for WC. However, the incompletely formed rod like/particle aggregates showed presence of mixed fringes of both (002) and (020) planes. The particle agglomerates had fringes with a d-spacing of 0.371 nm, which matches with the (020) plane of monoclinic WO_3 as reported in references.[43,45] The regular intensities of bright spots in the SAED pattern and the monocrystalline surface character both were more profound in case of WC compared to WT.

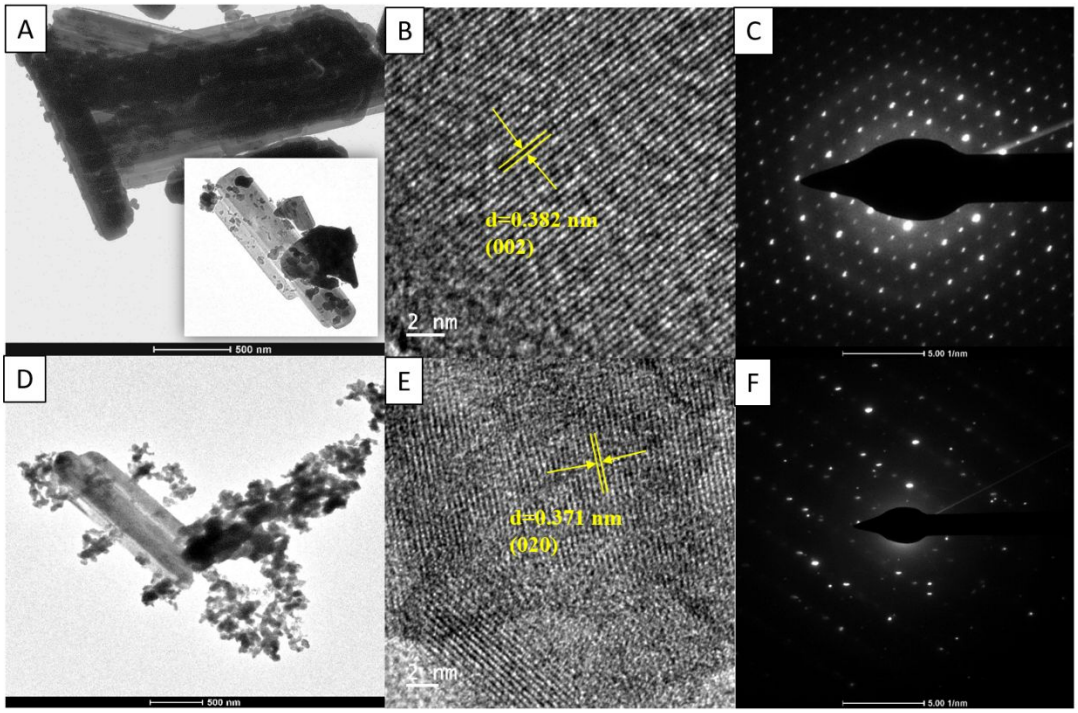

Figure 2: The TEM, HRTEM and SAED analysis (A-C) for WC and (D-F) for WT respectively

Further analysis of the surface crystal structure and growth patterns of different planes in the synthesized WO_{3-x} morphologies were performed using X- ray powder diffractometer. Fig. 3 A-E represents the XRD pattern of all the synthesized WO_{3-x} morphologies. All the WO_{3-x} samples indicate the formation of a stable monoclinic phase, with peaks appearing at 2θ value of 22.7, 23.5, 24.2, 26.5, 28.8, 32.8, 33.6, 34.1, 35.2, 41.2, 41.8, 45.1, 47.1, 49.8, 50.1 and 55.4 having miller indices (002), (020), (200), (120), (-112), (022), (-202), (202), (122), (-222), (222), (004), (040), (140), (-114) and (420) respectively (P21/n, JCPDS # 43-1035) and as reported in.[15,46,47] Since, the observed peaks are intense, sharp and of narrow width with no peaks of secondary phases present, it can be thus concluded that the synthesized WO_{3-x} is of high surface purity and crystallinity.

It is interesting to note that, the obtained WO_{3-x} morphologies have significant differences in the relative percentage distribution of (002), (200) and (020) facets (shown as a separate subset at R.H.S in Fig. 3). A comparative analysis of the ratio of major peaks with miller indices (002) : (020) : (200) are as follows: WU (1.5 : 1.26 : 1), WC (1.59 : 1.31 : 1), WSC (0.99 : 1.05 : 1), WN (0.95 : 0.92 : 1) and WT (0.92 : 0.99 : 1) . It is evident that both urea and carbohydrazide have the highest intensity ratio of (002) plane which is an indicative of the fact that, the profound growth of WO_{3-x} nanorods as observed in SEM and TEM, is facilitated by the systematic tailored growth of WO_{3-x} particles along the (002) plane, leading to a highly monocrystalline nanorod surface. On the contrary, XRD pattern of WO_{3-x} obtained using CH- substituted ureas, showed a significant decrease in the (002) plane intensity with increase in the degree of CH- substitution from N-methyl urea to tetramethyl urea. It appears that with the increase in the number of bulky methyl groups, the steric effect also increases, which facilitates the growth of WO_{3-x} particles along the (020) and (200) plane instead of (002). These (020) and (200) planes possibly lack the flexibility for tailored growth into one dimensional structure and therefore results in incompletely formed nanorods or nanoparticle agglomerates. The (002) plane is not only important for building 1D WO_{3-x} nanostructures as observed above but is even more significant in improving the electrochemical activity of WO_{3-x} which has been confirmed through electro capacitive measurements and shall be discussed later in detail in section 3.2

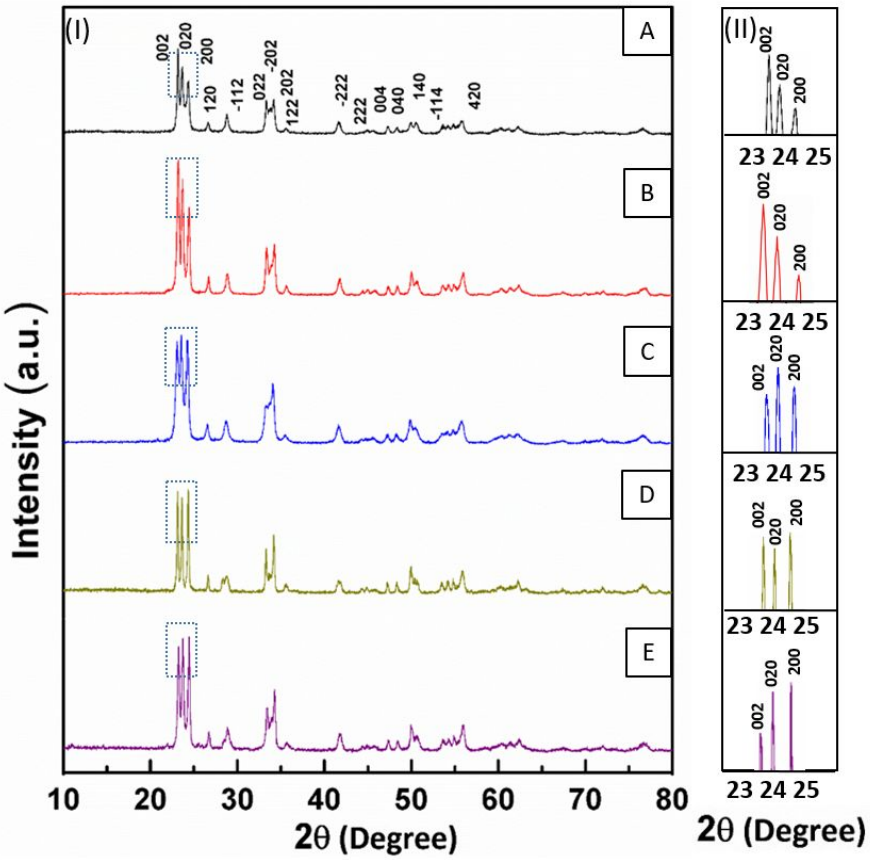

Figure 3: XRD patterns of WO_{3-x} synthesized with (A) urea[40] (*adapted from ref. 40 with permission from The Royal Society of Chemistry*) (B) carbohydrazide (C) semicarbazide (D) N-methylurea and (E) tetramethylurea. (I) overlay of XRD patterns and (II) is a magnified subset of rectangular area in (I)

It is possible that, such a transformation from 0D particles into 1D rods could be accompanied by structural defects during solid state crystal growth of WO_{3-x} nanorods. Such defects could also result in induced partial non stoichiometry in molecular composition leading to formation of WO_{3-x}. To obtain more information on the chemical composition and relative distribution of oxidation states of the synthesized WO_{3-x} nanostructures, X-ray photoelectron spectroscopy (XPS) was employed to analyze representative samples of fully grown nanorods (WC, WU) and mixed rod-particles agglomerates (WT). The XPS spectra (Fig. 4, A-A4) is of WC while that of WU is

presented in Fig. S1 in the supplementary material. All these WO_{3-x} samples display the characteristic W4f peaks located at 35.53 eV and 37.68 eV which can be attributed to W $4f_{7/2}$ and W $4f_{5/2}$, respectively, these peaks result from the spin orbit splitting of $4f_{7/2}$ with $4f_{5/2}$.[48] These two peaks are well separated and the peak fitting reveals the presence of majority of bulk tungsten in W^{6+} while 13-15 % in W^{5+} oxidation state, mostly on the surface of the material, in agreement with the observations of Tu et al.[30] and Qiu et al.[49] The O1s peak is located at 530.36 eV, which is ascribed to the W-O peak, and a shoulder peak at 532.62 eV is due to the oxygen in water molecules intercalated in the WO_{3-x} crystal structure.[48,50] The Na1s peak at 1071.71 eV consistent with the +1 oxidation state of sodium, is in small quantities leftover after centrifugal washing from the precursor, in agreement with the EDX results (Fig. 4 B). A minor C1s peak is observed at 284.92 eV due to the presence of adventitious carbon species from the instrument. Similar peaks are observed in case of WT as shown in Fig. 4 C-C4. The energy separations and the peak positions are in good agreement with the NIST XPS data base.[51] The percentage composition analysis of W^{6+}, W^{5+} and O1s peaks as presented in Table 1. This trend is also supported by the results of EDX analysis as shown in Fig. 4 B and D. The W4f analysis of XPS spectra reveals that the ratio of W^{5+}/W^{6+} is 0.17 for WC and 0.13 for WT which confirms that the nanorod surface has a greater magnitude of surface oxygen defects compared to particle agglomerates. Moreover, the relative distribution of the interstitial water is greater in WC compared to the rest of the catalysts. Therefore, the above findings clearly suggest that the NH- substitution in urea, enhance the presence of surface oxygen defects during the growth of nanorod structure, which can serve as active centers in electrified interfacial applications.[52] On the contrary, the inefficiency of CH-substituted ureas in forming nanorod structure, thus result in retaining the agglomerated particle morphologies with relatively lesser oxygen defects.

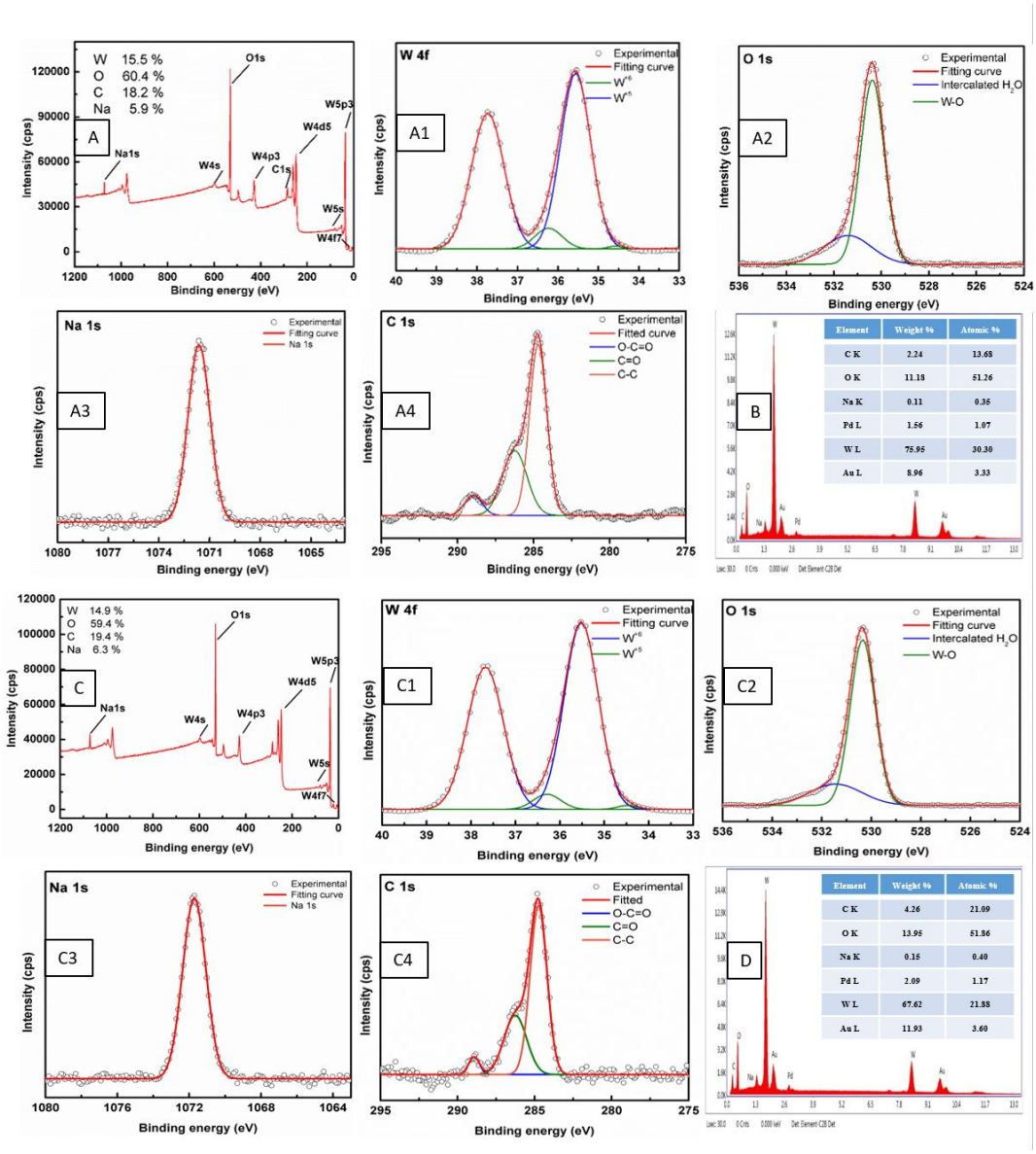

Figure 4: (A-A4) represents the XPS spectra and (B) EDX analysis of WO_{3-x} nanorods prepared using carbohydrazide, while (C-C4) represents the XPS spectra and (D) EDX analysis of WO_{3-x} particles prepared using tetramethylurea respectively.

Material	Narrow scan	Tungsten species	XPS area integration (%)	Area ratio W^{5+} / W^{6+}
WU	W 4f	W^{6+}	86.58	0.15
		W^{5+}	13.41	
	O 1s	W-O	78.45	
		Intercalated H_2O	21.55	
WC	W 4f	W^{6+}	85.66	0.17
		W^{5+}	14.34	
	O 1s	W-O	74.55	
		Intercalated H_2O	25.45	
WT	W 4f	W^{6+}	88.47	0.13
		W^{5+}	11.53	
	O 1s	W-O	78.88	
		Intercalated H_2O	21.01	

Table 1: The percentage of species obtained from the XPS peak area integration of narrow scan spectra

All the above findings and trends of SEM, HRTEM, XRD and XPS studies confirm our hypothesis that the type of NH- and CH- substitution in urea, significantly alters the growth mechanism of WO_{3-x} nanorods. This alteration in the growth mechanism could arise from the differences in the thermal decomposition processes of CH- and NH- substituted ureas. Therefore, thermogravimetric analysis were performed on the as synthesized metal precursor -CH/NH- substituted Urea-hybrid gels to obtain greater insight in the oxidation process.

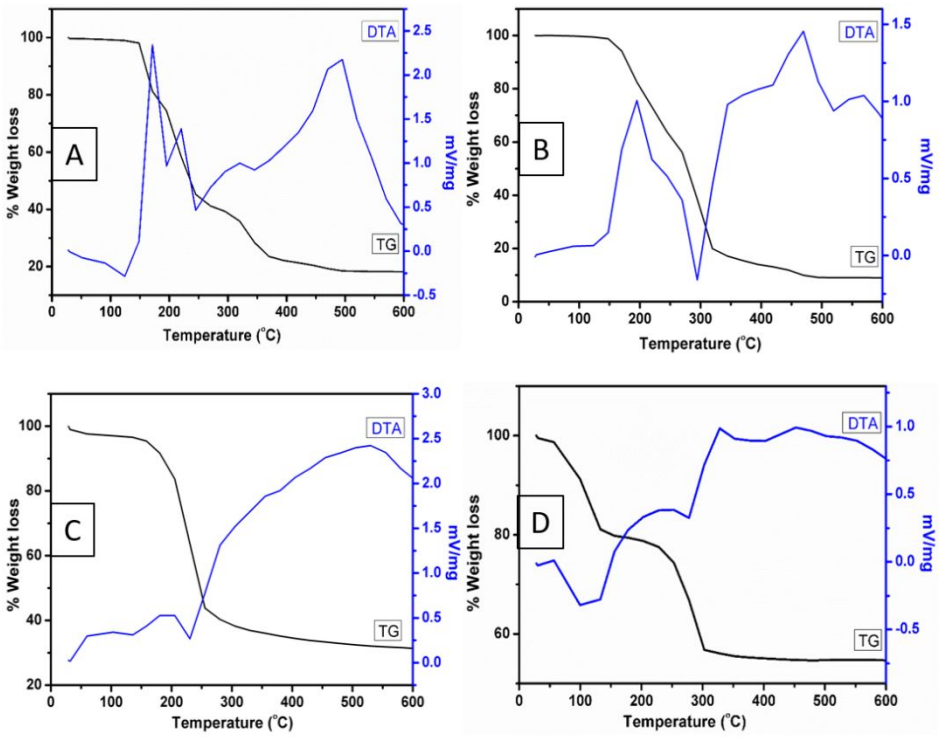

Figure 5: TG-DTA curve of the as-synthesized mixture of (A) tungstic acid– carbohydrazide, (B) tungstic acid-semicarbazide (C) tungstic acid–N-methylurea and (D) tungstic acid–tetramethylurea hybrid gels.

Fig. 5 A-D represents the TG-DTA curve of the as synthesized tungstic acid-substituted urea hybrid gels. The initial weight loss observed below 150 ℃, corresponding to an endothermic peak around 100-110 ℃ in DTA, is attributed to the loss of physically adsorbed water and is common in all the four samples. However, striking differences are observed in the subsequent rate of decomposition of hybrid gels based on the type of substitution in the urea. For instance, in case of NH- substituted carbohydrazide and semicarbazide modified precursor gels, decomposition starts during its melting process i.e. 159 ℃ for carbohydrazide and 170 ℃ for semicarbazide. Upon further heating, a major weight loss is observed which is attributed to the combustion of, at first the excess uncoordinated carbohydrazide/semicarbazide, followed by the combustion of those

molecules coordinated with tungstic acid gel, which requires relatively higher temperatures for complete removal.[40] The decomposition of carbohydrazide in particular is known to facilitate the in situ formation of hydrazine.[53] This step wise release of in situ generated hydrazine (which is an efficient fuel) and its subsequent exothermic decomposition into NO_x and CO_2 would allow controlled release of excess energy for complete and profound crystal growth of WO_{3-x} nanorods. This controlled combustion of in situ generated hydrazine also avoids the unwanted nanoparticle sintering effect observed by several research groups, when hydrazine is added ex situ as a fuel.[33] More importantly, the in situ reducing atmosphere so created could also facilitate partial reduction of the W^{6+} to W^{5+} on the nanorod surface resulting in formation of WO_{3-x} surface oxide as confirmed by XPS studies. A similar effect can be observed in urea modified precursor gels, with urea decomposition producing NH_3 and CO.[54]

On the contrary, the corresponding decomposition patterns of metal precursor gels modified with CH-substituted ureas is relatively rapid and reaches a stable weight loss at around 400 ^oC compared to 500 ^oC in case of NH-substituted urea modified precursor gels. Such a rapid decomposition possibly does not provide sufficient kinetic energy for controlled reduction of W^{6+} and complete growth of nanorod structure. Moreover, it induces sintering and agglomeration of nanoparticles as observed in SEM and TEM analysis, thus reducing the number of accessible active redox centers. The FTIR analysis were also performed wherein characteristic peaks due to C-H, C-N, N-H, N-N, C=O and O-H, stretching frequencies of the corresponding substituted urea modified hybrid gels were observed (see Fig. S2 in supplementary material). These peaks get eliminated upon calcination at 550 ^oC in air, giving rise to O-W-O and W=O vibrations at 672 cm^{-1} and 837 cm^{-1} leading to the formation of WO_{3-x} in agreement with XRD and XPS studies.

3.1 GROWTH MECHANISM OF WO_{3-x} NANORODS: The detailed growth mechanism of protonated urea induced transformation of nanoparticles into 1D WO_{3-x} nanorods using the nucleation-growth-assembly route has already been explained in our earlier report,[40] which is also applicable to the substituted ureas presented here. Therefore, only a brief explanation with modifications based on new findings of this study is presented here. The synthesis parameters were optimized and the calcination temperatures of < 650 ℃ were observed to be optimum for nanorod growth. At temperatures > 650 ℃ the nanorods tend to sinter leading to structural deformation. Also the metal to substituted urea ratio of 1:6 was confirmed to be the ideal ratio for the growth of WO_{3-x} nanorods. As explained earlier, the key factors for the generation of nanorods is the formation of colloidal tungstic acid gel particles and its subsequent interaction with NH-substituted, O-protonated urea. The supersaturation force of acidic medium acts as the driving force at the nucleation step, forming larger crystals of WO_3 nanoparticles.[40] The capping tendency of O-protonated, NH-substituted ureas becomes crucial at this stage as it serves as a structure directing motif to force one dimensional growth of WO_{3-x} crystallites.[40] Moreover, the tailoring of nanocrystallites into 1D nanorods requires a greater activation energy along with other kinetic and thermodynamic requirements. The relative differences in the combustion rates and combustion energies of substituted ureas vary in the order tetramethylurea > N-methylurea > carbohydrazide > semicarbohydrazide > urea.[55–58] Therefore, their differential combustion rates as observed in TG-DTA, induces variation in the percentage distribution of (002):(020):(200) surface planes in the nanocrystallites. This possibly results in the variation in number of nanocrystallites being stitched together into 1D nanorods along the preferred (002) plane. The in situ formation of hydrazine in case of NH- substituted ureas, possibly allows controlled release of excess energy to effectively overcome these requirements, which are accompanied by induction of partial surface

oxygen vacancies in the lattice during the crystal growth of nanorods. This has been further confirmed by performing a control experiment with hydrazine which did not lead to the formation of nanorods. This was expected due to the absence of the O-protonation center in hydrazine. Moreover, the uncontrolled explosive combustion of hydrazine leads to heavy sintering of the nanoparticles. The extent of W^{6+} partial reduction tendency is in the order of carbohydrazide > semicarbazide > urea > N-methylurea > tetramethylurea in good agreement with the XPS results. In a recent study by Tu et al.[30] a series of WO_{3-x} nanorods with surface oxygen vacancies were obtained via thermally treating pre-synthesized nanorods in H_2 atmosphere.[30] The chemical reactions leading to the production of WO_{3-x} nanorods in the present work can be described as follows:

$$Na_2WO_4 + 2HCl + nH_2O \rightarrow H_2WO_4.nH_2O + 2NaCl \qquad (1)$$

$$H_2WO_4.nH_2O + m(-C=NH_2^+)(\text{imminium cation}) \xrightarrow{\Delta} WO_{3-x} + mNH_3 + mCO_2 + (n+m)H_2O \qquad (2)$$

The second crucial factor to be considered here is the requirement of self-association of one-dimensional hydrogen bonded chains of the building units, which are the prerequisites for designing one dimensional nanomaterials. In order to form these one-dimensional hydrogen bonded chains, a good complementarity must be maintained between both the protonated carbonyl oxygen as well as, at the NH groups. The increase in degree of methylation from N-methylurea to tetramethyl urea therefore decreases this synergy and thereby is unable to produce WO_{3-x} nanorods. On the contrary, carbohydrazide satisfies both the thermodynamic requirements of energy and nucleation growth kinetics for complete growth of nanorods as observed in SEM and TEM studies. The schematic illustration of the above plausible mechanism is presented in Fig. 6. The effect of all the above morphological and chemical changes induced in WO_{3-x} nanostructures due to the CH- and NH- substitution in ureas, on the interfacial processes such as reversible H^+

ion intercalation in WO_{3-x} with reference to supercapacitor application, has been further investigated and shall be discussed in the next section.

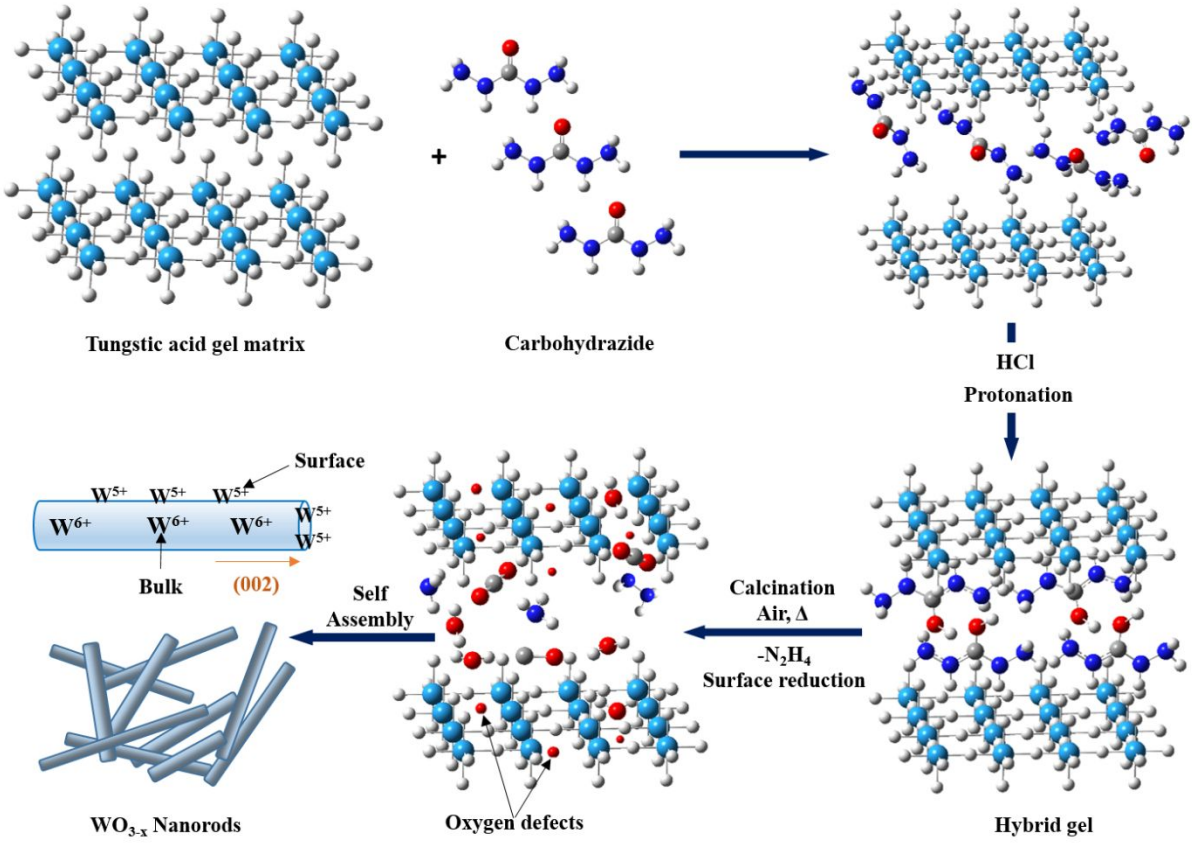

Figure 6: Schematic illustration of the plausible WO_{3-x} nanorod growth mechanism with in situ induction of partial surface oxygen vacancies during the calcination of tungstic acid-carbohydrazide precursor gels in air at 550°C.

3.2 ELECTROCAPACITIVE MEASUREMENTS:

The investigation of interfacial processes in order to highlight the merits of NH- and CH-substitution in urea to generate WO_{3-x} architectures, was carried out using cyclic voltammetry (CV), galvanostatic charge discharge (GCD) and electrochemical impedance spectroscopy (EIS) tests. Fig. 7 A shows CV measurements of WC in a three electrode system with 0.5 M H_2SO_4 electrolyte and at a scan rate of 50 mV s^{-1} in a potential window between -0.2 to 1.0 V (vs. Ag/AgCl) at 28°C ± 1°C after the 1st and 150th cycle. The nature of voltammogram can be understood as per the following Eq. 3.

$$WO_{3(\text{bleached})} + nH^+ + ne^- \leftrightarrow H_nWO_{3(\text{colored})} \qquad (3)$$

A typical cyclic voltammogram (as shown in Fig. 7 A and Fig. S3 in supplementary), shows an anodic peak at ~ -0.1 V vs Ag/AgCl due to the deintercalation of H^+ ions from the WO_{3-x} matrix.[59,60] However, as a consequence of continuous intercalation/deintercalation cycles, the WC modified electrodes showed a significant increase in voltammogram area, an observation similar to WU as reported in our previous work.[40] As observed from our XRD analysis (Fig. 3 A and B) both WC and WU nanorods have the dominance of (002) plane. The (002) plane of WO_{3-x} has

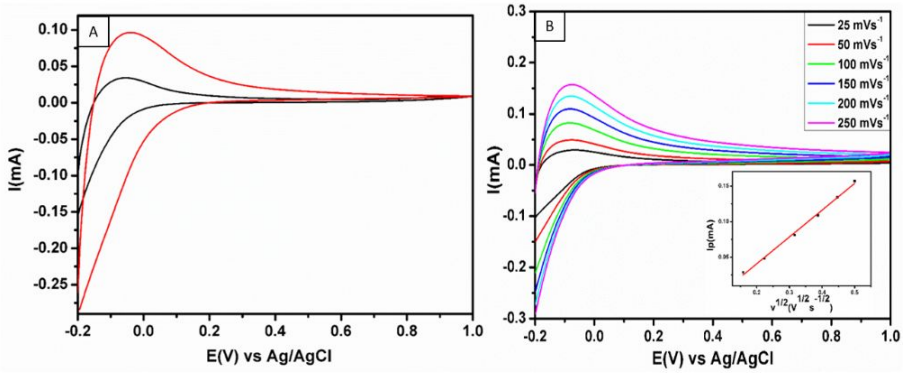

Figure 7: (A) Overlay of cyclic voltammograms recorded at WC modified glassy carbon electrodes in 0.5 M H_2SO_4 solution at a scan rate of 50 mV s^{-1} after the 1st (Black) and 150th (Red) cycle. (B) Scan rate dependent CV curves for WC nanorods with an inset depicting the chart for current I_p vs. square root of scan speed $v^{1/2}$

been reported several times as being the reason for improved electro catalytic activity.[61] Valdés et al. using density functional theory (DFT) calculations has reported that the photo oxidation of water on gamma WO_3 surfaces requires an overpotential of 1.10 V for (020) and 1.05 V for (002) plane.[62] Xie et al. and Zheng et al. have established the surface energy order in WO_3 as (002) (1.56 J m^{-2}) > (020) (1.54 J m^{-2}) > (200) (1.43 J m^{-2}), which indicates that (200) being the most stable and (002) as the least stable and thereby making it the most reactive plane.[63,64] Guo et al. reported that in nanoporous WO_3, the preferential orientation of the (002) planes helps in improving electrode kinetics by providing better conditions for the adsorption and redox reaction of pollutants compared to the (020) planes.[65] To understand the improved kinetics associated with the (002) surface dominant WO_{3-x}, the diffusion coefficient (D_0) for H^+ ions was estimated by performing scan rate dependent study of the different WO_{3-x} modified glassy carbon electrodes.

Fig. 7 B and S4 shows the CVs of the synthesized WO_{3-x} nanorods at scan rates from 25 to 250 mV s^{-1}. The oxidation current increases with increasing scan rate. Inset shows the graph of oxidation peak current vs square root of scan rate, which exhibits a linear regression with R^2 value of 0.99, which is an indication that there is no surface poisoning of the electrode surface. From CV measurements at different scan rates, the values of anodic peak current (I_p) were obtained. From the slope of square root of scan rate ($v^{1/2}$) versus the anodic peak current (I_p) graph, the diffusion coefficient of H^+ ions is calculated using the Randles-Sevcik equation[66] (Eq. 4) at 298 K.

$$I_p = 2.69 \times 10^5 A C_0 D_0^{1/2} n^{3/2} \upsilon^{1/2} \qquad (4)$$

In the above equation (4), 2.69×10^5 is a constant, A is the area of electrode, C_0 is the electrolyte concentration and n is the amount of electrons transferred during the reaction (herein, $n = 1$). The calculated D_0 values of WC is 9.89×10^{-9} cm^2 s^{-1} and WU is 8.38×10^{-9} cm^2 s^{-1},[40] while that of

WN = 1.67 × 10^{-9} cm^2 s^{-1}, WSC= 1.43 × 10^{-9} cm^2 s^{-1} and WT = 1.39 × 10^{-10} cm^2 s^{-1} were almost identical within the error limits (refer Fig. S4 in supplementary data file). It is to be noted here that, the D_0 values of fully grown rods (WC and WU) are greater by a factor of 12 times compared to partially formed rod-particles agglomerates (WSC, WN and WT) as listed above. The greater D_0 values for WC and WU indicate the ease with which the H^+ ions can diffuse in as well as out of the WO_{3-x} matrix. The D_0 values are comparable to work of Xiao et al.[66] wherein a value of 1.91 × 10^{-9} cm^2 s^{-1} has been reported for porous WO_3 electrode and to the work of Ghosh et al.[16] who have reported a value of 2.27 × 10^{-10} cm^2 s^{-1} for hexagonal WO_3. To understand the reason behind such an enormous difference in D_0 values between the two distinct morphologies, the electroactive areas of the materials were estimated using the Cottrell equation (Eq. 5) in a ferrocyanide reversible redox system.

$$(i)_t = \frac{nFAD_0^{1/2}C^*}{\Pi^{1/2}t^{1/2}} \qquad (5)$$

where $(i)_t$ is the peak current (in A), n denotes the number of electrons, F = 96,485 C mol^{-1} is the Faraday constant, A represents the electroactive surface area of the electrode (cm^2), C^* represents bulk concentration of the analyte (mol cm^{-3}) and t denotes the time (s). WC resulted in the highest electroactive area of 0.191 cm^2 followed by WU (0.169 cm^2) while WN, WSC had relatively lower electroactive areas of 0.163 cm^{-2}, 0.119 cm^{-2} respectively with WT (0.045 cm^{-2}) being the lowest electroactive surface. The results of BET surface area analysis were in trend with the electroactive area results and were observed to be 7.0, 5.3, 4.0, 3.9 and 3.5 m^2 g^{-1} for WC, WU, WN, WSC and WT respectively although the trend may as well be just a coincidence. The decrease in the electroactive areas from the nanorods (WC with W^{5+}/W^{6+} = 0.17) to particle agglomerates (WT

with $W^{5+}/W^{6+} = 0.13$) can be understood as a consequence of reduction in surface oxygen defects and decreased presence of intercalated H_2O as observed from the XPS analysis (Table 1).

Electrode stability is also an important parameter for evaluating the performance of capacitor electrode materials.[67] We observed that the morphology of the electrode material had an impact on its stability. The stability of the modified electrodes were studied using chronoamperometry and is presented in Fig. S5 in supplementary data file. It was observed that the electrode films prepared from fully grown nanorod morphologies were significantly more stable than those prepared with rod-particle agglomerates. Subsequently, all the synthesized morphologies were subjected to capacitance measurements. The CVs at different scan rates (20-120 mV s^{-1}) for WC are presented in Fig. 8 A, and for WSC, WN and WT modified electrodes are presented Fig. S6 in supplementary data file. As the scanning rate was increased, the shape of CV curves hardly changed, indicative of the excellent electrochemical reversibility and high power performance.[68] The area specific capacitance of different modified electrodes as a function of scan rate (20-120 mV s^{-1}) were calculated as tabulated in table S1 in the supplementary data file. The calculation of specific capacitance reveals the highest area specific capacitance for WC electrodes (105 mF cm^{-2} at 20 mV s^{-1}) and the lowest for WT electrodes (35 mF cm^{-2} at 20 mV s^{-1}). Moreover, specific capacitance value (C_s) decrease with the increase in scan rate as expected, since the H^+ ions do not have enough time to intercalate at the active centers at higher scanning rates.[69-70]

Furthermore, the galvanostatic charge discharge analysis were performed at variable current densities from 1 to 3 mA cm^{-2} as shown in Fig. 8B and Fig. S7 in supplementary data file respectively. The maximum discharge time was observed for WC showing the highest specific capacitance which was consistent with the results of CV tests. Area specific capacitance from the GCD analysis was calculated using the equation (6).[71]

$$C_{sp} = \frac{I \times \Delta t}{S \times \Delta V} \qquad (6)$$

where I is the constant discharge current, Δt represents the discharge time, S is the geometric area of the electrode and ΔV represents the potential drop during the discharge time. The observed specific capacitance is mentioned in Table 2.

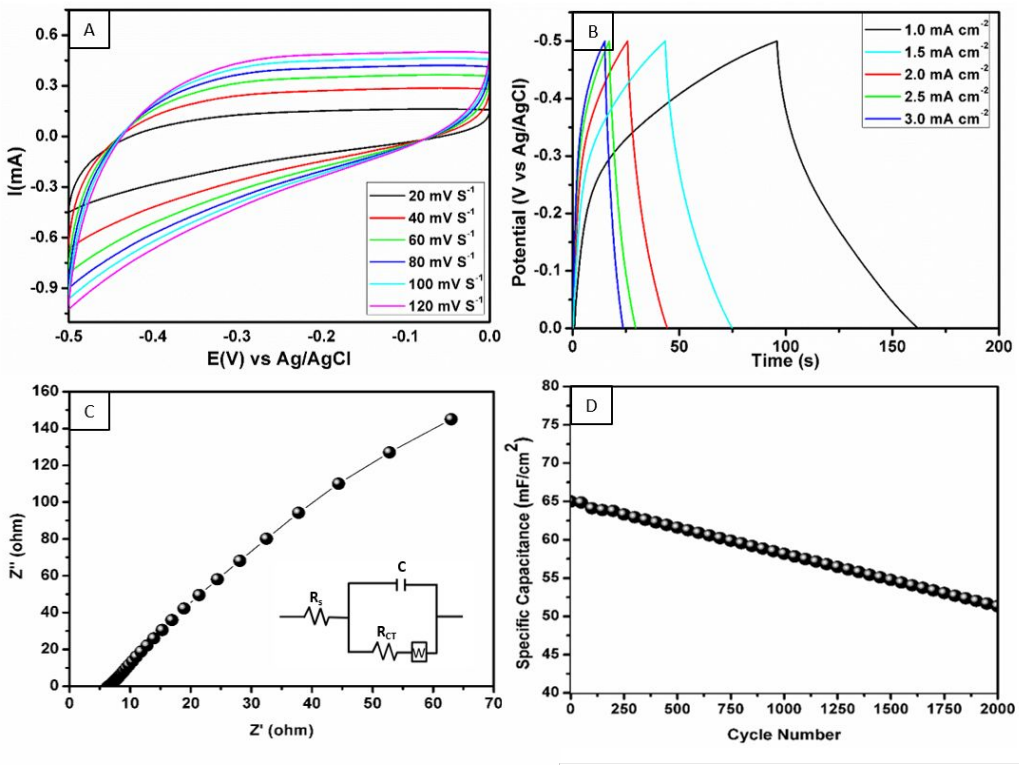

Figure 8: (A) Scan rate dependent CV curves (B) Galvanostatic charge discharge (GCD) curves at different current densities (C) Nyquist plot in the frequency range of 1 Hz to 1 MHz and (D) Cycling stability from GCD at a current density of 2.5 mA cm^{-2} for WC nanorods.

Current density (mA cm^{-2})	Specific capacitance (mF cm^{-2})				
	WC	WU	WN	WSC	WT
1	132	76	66	34	18.6
1.5	92.9	59.9	56.9	23.9	14.1
2	76	52	48	20	12.4
2.5	64.9	49.9	44.9	19.9	10.9
3	53.9	41.9	25.9	11.9	9.6

Table 2: Table showing specific capacitances of materials at variable current densities obtained from the GCD analysis

The highest value of area specific capacitance of 132 mF cm^{-2} was obtained for WC at a current density of 1 mA cm^{-2} and it decreases with the increase in current density from 1 to 3 mA cm^{-2}. The capacitance retained was in the range of 70% - 80% for WC and WU for the current density rise of 0.5 mA cm^{-2}. Moreover electrode stability was also investigated using GCD for over 2000 cycles at a current density of 2.5 mA cm^{-2} and film stability of 80% was observed for WC nanorods as evident from Fig. 8D. The slight decay can be attributed to the loss of active material during electrochemical cycling. The results of specific capacitance obtained are in par with the literature reports wherein Huang et al.[72] has reported the capacitance of 62.4 mF cm^{-2} at a scan rate of 20 mV s^{-1} for nanostructured WO_3 composite, Jin et al.[73] has reported the volumetric capacitance of 59.7 mF cm^{-3} at a current density value of 0.5 mA cm^{-2} for porous WO_3 electrodes, Tian et al.[74] has reported the specific capacitance of 25 mF cm^{-2} at the current density of 0.08 mA cm^{-2} for $W_{18}O_{49}$/PANI composites etc. The electrochemical behavior at the electrode electrolyte interface was studied further using EIS analysis. An equivalent circuit was identified and is presented in the

inset in Fig. 8 C and S8. The Nyquist plots (Fig. 8 C and S8) from the EIS studies are observed to be consisting of a relatively straight line in the low frequency region and a semicircle in the high frequency region. The straight line can be ascribed to the diffusion of ions from the electrolyte to the WO_{3-x} modified electrode surface while the semicircle can be ascribed to the charge-transfer resistance (R_{ct}).[71] From the Nyquist plots solution resistance (R_S) for WC, WU, WN, WSC and WT was found to be 6.37, 7.19, 12.71, 14.42 and 19.65 Ω respectively. The lower value of R_S suggested good electrical conductivity and better electrode contact observed in the case of WO_{3-x} nanorods. The highest value of capacitance and improved performance measured for WC and WU electrodes over WN, WSC and WT electrodes is a cumulative result of presence of more profound active sites due to the greater presence of W^{5+}/W^{6+} state, the presence of more intercalated H_2O and presence of active (002) plane in the WO_{3-x} observed through SEM, HRTEM and XPS studies.

4. CONCLUSIONS

The role of NH- and CH- substitution in urea to induce morphological and chemical changes in the synthesized WO_{3-x} nanostructures using direct calcination of tungstic acid-substituted urea hybrid gels was investigated. The NH- substitution was found to promote the one dimensional nanorod growth, preferentially along (002) plane. It further facilitated the creation of surface oxygen defects, leading to the formation of partially reduced WO_{3-x} nanorods with surface distribution of W^{5+}/W^{6+} redox states. The synthesized WO_{3-x} materials were investigated for potential application in charge storage systems wherein, the electrified interfacial processes were investigated using cyclic voltammetry and galvanostatic charge discharge analysis. As a result of the abundant (002) surface planes and the W^{5+}/W^{6+} redox surface states, the WO_{3-x} nanorods synthesized using carbohydrazide showed the highest area specific capacitance of 132 mF cm^{-2} at the current density of 1 mA cm^{-2}, with excellent capacitance retention compared to the WO_{3-x}

obtained using CH- substituted ureas. This study therefore opens up a new doorway towards utilizing protonated, NH- substituted ureas as promising novel, self-assembly directing motifs, for scalable synthesis of 1D nanostructured materials for application in charge storage systems.

5. ASSOCIATED CONTENT

Supporting Information

XPS spectra of WU nanorods, IR spectra of synthesized gel and WO_{3-x} obtained after calcination, Overlay of CV curves at a fixed scan rate after continuous cycling, Scan rate dependent CV curves for investigating diffusion coefficients, Film stability investigated using chronoamperometry, Scan rate dependent CV curves for investigating the capacitive performance, GCD curves at different current densities, tabulated specific capacitances of materials at variable scanning rates and Nyquist plots.

6. ACKNOWLEDGEMENTS

The authors thank the following funding agencies for their financial support namely DST/INNO-INDIGO (DST/IMRCD/INNO-INDIGO/BIOCFD/2017(G), DST SERB (ECR/2015/000047), UGC New Delhi, at the level of DSA-I under the Special Assistance Program (SAP) (F. No. 540/14/DSA-I/2015/(SAP-I)), DST-FIST and nano mission project No. SR/NM/NS-86/2009. R.X.F at PTB Germany was supported by INNO INDIGO Partnership Programme (IPP)-IPP2_ST-082. The authors express their sincere gratitude to late Dr. Pankaj R. Singh for establishing electrochemical testing facilities at Goa University which were utilized for this research work.

7. REFERENCES

(1) Jiao, Z.; Wang, J.; Ke, L.; Sun, X. W.; Demir, H. V. Morphology-Tailored Synthesis of Tungsten Trioxide (Hydrate) Thin Films and Their Photocatalytic Properties. *ACS Appl. Mater. Interfaces* **2011**, *3* (2), 229–236.

(2) Ray, C.; Pal, T. Recent Advances of Metal-Metal Oxide Nanocomposites and Their Tailored Nanostructures in Numerous Catalytic Applications. *J. Mater. Chem. A* **2017**, *5* (20), 9465–9487.

(3) Sun, W.; Yeung, M. T.; Lech, A. T.; Lin, C. W.; Lee, C.; Li, T.; Duan, X.; Zhou, J.; Kaner, R. B. High Surface Area Tunnels in Hexagonal WO_3. *Nano Lett.* **2015**, *15* (7), 4834–4838.

(4) Mitchell, J. B.; Lo, W. C.; Genc, A.; Lebeau, J.; Augustyn, V. Transition from Battery to Pseudocapacitor Behavior via Structural Water in Tungsten Oxide. *Chem. Mater.* **2017**, *29* (9), 3928–3937.

(5) Liang, L.; Zhang, J.; Zhou, Y.; Xie, J.; Zhang, X.; Guan, M.; Pan, B.; Xie, Y. High-Performance Flexible Electrochromic Device Based on Facile Semiconductor-To-Metal Transition Realized by $WO_3.2H_2O$ Ultrathin Nanosheets. *Sci. Rep.* **2013**, *3*, 1–8.

(6) Wen, R. T.; Niklasson, G. A.; Granqvist, C. G. Sustainable Rejuvenation of Electrochromic WO_3 Films. *ACS Appl. Mater. Interfaces* **2015**, *7* (51), 28100–28104.

(7) Xie, Y.; Wu, E.; Hu, R.; Qian, S.; Feng, Z.; Chen, X.; Zhang, H.; Xu, L.; Hu, X.; Liu, J.; Zhang, D. Enhancing Electronic and Optoelectronic Performances of Tungsten Diselenide by Plasma Treatment. *Nanoscale* **2018**, *10* (26), 12436–12444.

(8) Shao, D.; Yu, M.; Lian, J.; Sawyer, S. Optoelectronic Properties of Three Dimensional WO_3

Nanoshale and Its Application for UV Sensing. *Opt. Mater.* **2014,** *36* (5)*, 1002-1005*.

(9) Li, X. L.; Lou, T. J.; Sun, X. M.; Li, Y. D. Highly Sensitive WO_3 Hollow-Sphere Gas Sensors. *Inorg. Chem.* **2004**, *43* (17), 5442–5449.

(10) Godbole, R.; Godbole, V. P.; Alegaonkar, P. S.; Bhagwat, S. Effect of Film Thickness on Gas Sensing Properties of Sprayed WO_3 Thin Films. *New J. Chem.* **2017**, *41* (20), 11807–11816.

(11) Jelinska, A.; Bienkowski, K.; Jadwiszczak, M.; Pisarek, M.; Strawski, M.; Kurzydlowski, D.; Solarska, R.; Augustynski, J. Enhanced Photocatalytic Water Splitting on Very Thin WO_3 Films Activated by High-Temperature Annealing. *ACS Catal.* **2018**, *8* (11), 10573–10580.

(12) Liu, Y.; Li, J.; Li, W.; Yang, Y.; Li, Y.; Chen, Q. Enhancement of the Photoelectrochemical Performance of WO_3 Vertical Arrays Film for Solar Water Splitting by Gadolinium Doping. *J. Phys. Chem. C* **2015**, *119* (27), 14834–14842.

(13) Hunyadi, D.; Szilágyi, I. M.; Tóth, A. L.; Drotár, E.; Igricz, T.; Pokol, G. Investigating the Solid-Gas Phase Reaction between WO_3 powder, NH_3 and H_2O Vapors to Prepare Ammonium Paratungstate. *Inorganica Chim. Acta* **2016**, *444*, 29–35.

(14) Nadji, L.; Massó, A.; Delgado, D.; Issaadi, R.; Rodriguez-Aguado, E.; Rodriguez-Castellón, E.; López Nieto, J. M. Gas Phase Dehydration of Glycerol to Acrolein over WO_3-Based Catalysts Prepared by Non-Hydrolytic Sol-Gel Synthesis. *RSC Adv.* **2018**, *8* (24), 13344–13352.

(15) Nagy, D.; Nagy, D.; Szilagyi, I. M.; Fan, X. Effect of the Morphology and Phases of WO_3

Nanocrystals on Their Photocatalytic Efficiency. *RSC Adv.* **2016**, *6* (40), 33743–33754.

(16) Ghosh, K.; Roy, A.; Tripathi, S.; Ghule, S.; Singh, A. K.; Ravishankar, N. Insights into Nucleation, Growth and Phase Selection of WO_3: Morphology Control and Electrochromic Properties. *J. Mater. Chem. C* **2017**, *5* (29), 7307–7316.

(17) Kim, H.; Bonsu, R. O.; Odonohue, C.; Korotkov, R. Y.; McElwee-White, L.; Anderson, T. J. Aerosol-Assisted Chemical Vapor Deposition of Tungsten Oxide Films and Nanorods from Oxo Tungsten(VI) Fluoroalkoxide Precursors. *ACS Appl. Mater. Interfaces* **2015**, *7* (4), 2660–2667.

(18) Kadir, R. A.; Zhang, W.; Wang, Y.; Ou, J. Z.; Wlodarski, W.; O'Mullane, A. P.; Bryant, G.; Taylor, M.; Kalantar-Zadeh, K. Anodized Nanoporous WO_3 Schottky Contact Structures for Hydrogen and Ethanol Sensing. *J. Mater. Chem. A* **2015**, *3* (15), 7994–8001.

(19) Zhang, H.; Li, Y.; Duan, G.; Liu, G.; Cai, W. Tungsten Oxide Nanostructures Based on Laser Ablation in Water and a Hydrothermal Route. *CrystEngComm* **2014**, *16* (12), 2491–2498.

(20) Wang, J.; Khoo, E.; Lee, P. S.; Ma, J. Controlled Synthesis of WO_3 Nanorods and Their Electrochromic Properties in H_2SO_4 Electrolyte. *J. Phys. Chem. C* **2010**, *113*, 9655–9658.

(21) Nayak, A. K.; Sohn, Y.; Pradhan, D. Facile Green Synthesis of $WO_3 \cdot H_2O$ Nanoplates and WO_3 Nanowires with Enhanced Photoelectrochemical Performance. *Cryst. Growth Des.* **2017**, *17* (9), 4949–4957.

(22) Ji, Y.; Yang, Y.; Lee, S. K.; Ruan, G.; Kim, T. W.; Fei, H.; Lee, S. H.; Kim, D. Y.; Yoon, J.; Tour, J. M. Flexible Nanoporous WO_{3-x} Nonvolatile Memory Device. *ACS Nano* **2016**,

10 (8), 7598–7603.

(23) Albanese, E.; Di Valentin, C.; Pacchioni, G. H_2O Adsorption on WO_3 and WO_{3-x} (001) Surfaces. *ACS Appl. Mater. Interfaces* **2017**, *9* (27), 23212–23221.

(24) Duan, G.; Chen, L.; Jing, Z.; De Luna, P.; Wen, L.; Zhang, L.; Zhao, L.; Xu, J.; Li, Z.; Yang, Z.; Zhou, R. Robust Antibacterial Activity of Tungsten Oxide (WO_{3-x}) Nanodots . *Chem. Res. Toxicol.* **2019**, *32* (7), 1357–1366.

(25) Johansson, M. B.; Mattsson, A.; Lindquist, S. E.; Niklasson, G. A.; Österlund, L. The Importance of Oxygen Vacancies in Nanocrystalline WO_{3-x} Thin Films Prepared by DC Magnetron Sputtering for Achieving High Photoelectrochemical Efficiency. *J. Phys. Chem. C* **2017**, *121* (13), 7412–7420.

(26) Wang, W.; Janotti, A.; Van De Walle, C. G. Role of Oxygen Vacancies in Crystalline WO_3. *J. Mater. Chem. C* **2016**, *4* (27), 6641–6648.

(27) Li, Y.; Tang, Z.; Zhang, J.; Zhang, Z. Defect Engineering of Air-Treated WO_3 and Its Enhanced Visible-Light-Driven Photocatalytic and Electrochemical Performance. *J. Phys. Chem. C* **2016**, *120* (18), 9750–9763.

(28) Lee, S.; Lee, Y.-W.; Kwak, D.-H.; Kim, M.-C.; Lee, J.-Y.; Kim, D.-M.; Park, K.-W. Improved Pseudocapacitive Performance of Well-Defined WO_{3-x} Nanoplates. *Ceram. Int.* **2015**, *41* (3), 4989–4995.

(29) Bao, K.; Mao, W.; Liu, G.; Ye, L.; Xie, H.; Ji, S.; Wang, D.; Chen, C.; Li, Y. Preparation and Electrochemical Characterization of Ultrathin WO_{3-x}/C Nanosheets as Anode Materials in Lithium Ion Batteries. *Nano Res.* **2017**, *10* (6), 1903–1911.

(30) Tu, J.; Lei, H.; Yu, Z.; Jiao, S. Ordered WO_{3-x} Nanorods: Facile Synthesis and Their Electrochemical Properties for Aluminum-Ion Batteries. *Chem. Commun.* **2018**, *54* (11), 1343–1346.

(31) Rinaldi, F. G.; Arutanti, O.; Arif, A. F.; Hirano, T.; Ogi, T.; Okuyama, K. Correlations between Reduction Degree and Catalytic Properties of WO_x Nanoparticles. *ACS Omega* **2018**, *3* (8), 8963–8970.

(32) Bignozzi, C. A.; Caramori, S.; Cristino, V.; Argazzi, R.; Meda, L.; Tacca, A. Nanostructured Photoelectrodes Based on WO_3 : Applications to Photooxidation of Aqueous Electrolytes. *Chem. Soc. Rev.* **2013**, *42* (42), 2228–2246.

(33) Li, F.; Ran, J.; Jaroniec, M.; Qiao, S. Z. Solution Combustion Synthesis of Metal Oxide Nanomaterials for Energy Storage and Conversion. *Nanoscale* **2015**, *7* (42), 17590–17610.

(34) Naik, A. P.; Salkar, A. V.; Majik, M. S.; Morajkar, P. P. Enhanced Photocatalytic Degradation of Amaranth Dye on Mesoporous Anatase TiO_2 : Evidence of C–N, N=N Bond Cleavage and Identification of New Intermediates. *Photochem. Photobiol. Sci.* **2017**, *16,* 1126-1138.

(35) Simic, V.; Bouteiller, L.; Jalabert, M. Highly Cooperative Formation of Bis-Urea Based Supramolecular Polymers. *J. Am. Chem. Soc.* **2003**, *125* (43), 13148–13154.

(36) Custelcean, R. Crystal Engineering with Urea and Thiourea Hydrogen-Bonding Groups. *Chem. Commun.* **2008**, *3*, 295–307.

(37) Koshti, V. S.; Thorat, S. H.; Gote, R. P.; Chikkali, S. H.; Gonnade, R. G. The Impact of Modular Substitution on Crystal Packing: The Tale of Two Ureas. *CrystEngComm* **2016**,

18 (37), 7078–7094.

(38) Sindt, A. J.; Smith, M. D.; Pellechia, P. J.; Shimizu, L. S. Thioureas and Squaramides: Comparison with Ureas as Assembly Directing Motifs for m -Xylene Macrocycles. *Cryst. Growth Des.* **2018**, *18* (3), 1605–1612.

(39) Morajkar, P.; B. Fernandes, J. A New Facile Method to Synthesize Mesoporous γ-Al_2O_3 of High Surface Area and Catalytic Activity. *Catal. Commun.* **2010**, *11*, 414–418.

(40) Salkar, A. V.; Naik, A. P.; Joshi, V. S.; Haram, S. K.; Morajkar, P. P. Designing a 3D Nanoporous Network Via Self-Assembly of WO_3 Nanorods for Improved Electrocapacitive Performance. *CrystEngComm* **2018**, *20* (42), 6683–6694.

(41) Varma, A.; Mukasyan, A. S.; Rogachev, A. S.; Manukyan, K. V. Solution Combustion Synthesis of Nanoscale Materials. *Chem. Rev.* **2016**, *116* (23), 14493–14586.

(42) Rajeswari, J.; Kishore, P.; Viswanathan, B.; Varadarajan, T. Facile Hydrogen Evolution Reaction on WO_3 Nanorods. **2007**, *4*, 496–503.

(43) Yin, J.; Cao, H.; Zhang, J.; Qu, M.; Zhou, Z. Synthesis and Applications of γ-Tungsten Oxide Hierarchical Nanostructures. *Cryst. Growth Des.* **2013**, *13* (2), 759–769.

(44) Nayak, A. K.; Verma, M.; Sohn, Y.; Deshpande, P. A.; Pradhan, D. Highly Active Tungsten Oxide Nanoplate Electrocatalysts for the Hydrogen Evolution Reaction in Acidic and near Neutral Electrolytes. *ACS Omega* **2017**, *2* (10), 7039–7047.

(45) Pokhrel, S.; Birkenstock, J.; Schowalter, M.; Rosenauer, A.; Mädler, L. Growth of Ultrafine Single Crystalline WO_3 Nanoparticles Using Flame Spray Pyrolysis. *Cryst. Growth Des.* **2010**, *10* (2), 632–639.

(46) Li, N.; Zheng, Y.; Wei, L.; Teng, H.; Zhou, J. Metal Nanoparticles Supported on WO_3 Nanosheets for Highly Selective Hydrogenolysis of Cellulose to Ethylene Glycol. *Green Chem.* **2017**, *19* (3), 682–691.

(47) Kalanur, S. S.; Hwang, Y. J.; Chae, S. Y.; Joo, O. S. Facile Growth of Aligned WO_3 Nanorods on FTO Substrate for Enhanced Photoanodic Water Oxidation Activity. *J. Mater. Chem. A* **2013**, *1* (10), 3479.

(48) Park, C. Y.; Seo, J. M.; Jo, H.; Park, J.; Ok, K. M.; Park, T. J. Hexagonal Tungsten Oxide Nanoflowers as Enzymatic Mimetics and Electrocatalysts. *Sci. Rep.* **2017**, *7*, 40928.

(49) Qiu, M.; Sun, P.; Shen, L.; Wang, K.; Song, S.; Yu, X.; Tan, S.; Zhao, C.; Mai, W. WO_3 Nanoflowers with Excellent Pseudo-Capacitive Performance and the Capacitance Contribution Analysis. *J. Mater. Chem. A* **2016**, *4* (19), 7266–7273.

(50) Castillero, P.; Rico-Gavira, V.; López-Santos, C.; Barranco, A.; Pérez-Dieste, V.; Escudero, C.; Espinós, J. P.; González-Elipe, A. R. Formation of Subsurface W^{5+} Species in Gasochromic Pt/WO_3 Thin Films Exposed to Hydrogen. *J. Phys. Chem. C* **2017**, *121* (29), 15719–15727.

(51) Arvizu, M. A.; Qu, H. Y.; Cindemir, U.; Qiu, Z.; Rojas-González, E. A.; Primetzhofer, D.; Granqvist, C. G.; Österlund, L.; Niklasson, G. A. Electrochromic WO_3 Thin Films Attain Unprecedented Durability by Potentiostatic Pretreatment. *J. Mater. Chem. A* **2019**, *7* (6), 2908–2918.

(52) Song, J.; Huang, Z. F.; Pan, L.; Zou, J. J.; Zhang, X.; Wang, L. Oxygen-Deficient Tungsten Oxide as Versatile and Efficient Hydrogenation Catalyst. *ACS Catal.* **2015**, *5* (11), 6594–6599.

(53) Cosper, D. R.; David, D. J. Copper-Catalyzed Autoxidation of Carbohydrazide: Kinetics and Mechanism. *Ind. Eng. Chem. Res.* **1990**, *29* (7), 1130–1136.

(54) Chen, P.; Qin, M.; Chen, Z.; Jia, B.; Qu, X. Solution Combustion Synthesis of Nanosized WO_x : Characterization, Mechanism and Excellent Photocatalytic Properties. *RSC Adv.* **2016**, *6* (86), 83101–83109.

(55) Yan, Q.-L.; Yang, Z.; Zhang, X.-X.; Lyu, J.-Y.; He, W.; Huang, S.; Liu, P.-J.; Zhang, C.; Zhang, Q.-H.; He, G.-Q.; Nie, F.-D. High Density Assembly of Energetic Molecules under the Constraint of Defected 2D Materials. *J. Mater. Chem. A* **2019**, *7* (30), 17806–17814.

(56) Kabo, G. Y.; Miroshnichenko, E. A.; Frenkel', M. L.; Kozyro, A. A.; Simirskii, V. V; Krasulin, A. P.; Vorob'eva, V. P.; Lebedev, Y. A. Thermochemistry of Alkyl Derivatives of Urea. *Bull. Acad. Sci. USSR, Div. Chem. Sci.* **1990**, *39* (4), 662–667.

(57) Tischer, S.; Börnhorst, M.; Amsler, J.; Schoch, G.; Deutschmann, O. Thermodynamics and Reaction Mechanism of Urea Decomposition. *Phys. Chem. Chem. Phys.* **2019**, *21* (30), 16785–16797.

(58) Dorofeeva, O. V.; Ryzhova, O. N.; Suchkova, T. A. Enthalpies of Formation of Hydrazine and Its Derivatives. *J. Phys. Chem. A* **2017**, *121* (28), 5361–5370.

(59) De Ribamar Martins Neto, J.; Torresi, R. M.; Cordoba De Torresi, S. I. Electrochromic Behavior of WO_3 Nanoplate Thin Films in Acid Aqueous Solution and a Protic Ionic Liquid. *J. Electroanal. Chem.* **2016**, *765*, 111–117.

(60) Kattouf, B.; Ein-Eli, Y.; Siegmann, A.; Frey, G. L. Hybrid Mesostructured Electrodes for Fast-Switching Proton-Based Solid State Electrochromic Devices. *J. Mater. Chem. C* **2013**,

1 (1), 151.

(61) Kwong, W. L.; Koshy, P.; Hart, J. N.; Xu, W.; Sorrell, C. C. Critical Role of (002) Preferred Orientation on Electronic Band Structure of Electrodeposited Monoclinic WO_3 Thin Films. *Sustain. Energy Fuels* **2018**, *2* (10), 2224–2236.

(62) Valḱs, Á.; Kroes, G. J. First Principles Study of the Photo-Oxidation of Water on Tungsten Trioxide (WO_3). *J. Chem. Phys.* **2009**, *130* (11), 114701.

(63) Xie, Y. P.; Liu, G.; Yin, L.; Cheng, H. M. Crystal Facet-Dependent Photocatalytic Oxidation and Reduction Reactivity of Monoclinic WO_3 for Solar Energy Conversion. *J. Mater. Chem.* **2012**, *22* (14), 6746–6751.

(64) Zheng, J. Y.; Haider, Z.; Van, T. K.; Pawar, A. U.; Kang, M. J.; Kim, C. W.; Kang, Y. S. Tuning of the Crystal Engineering and Photoelectrochemical Properties of Crystalline Tungsten Oxide for Optoelectronic Device Applications. *CrystEngComm* **2015**, *17* (32), 6070–6093.

(65) Guo, Y.; Quan, X.; Lu, N.; Zhao, H.; Chen, S. High Photocatalytic Capability of Self-Assembled Nanoporous WO_3 with Preferential Orientation of (002) Planes. *Environ. Sci. Technol.* **2007**, *41* (12), 4422–4427.

(66) Xiao, L.; Lv, Y.; Dong, W.; Zhang, N.; Liu, X. Dual-Functional WO_3 Nanocolumns with Broadband Antireflective and High-Performance Flexible Electrochromic Properties. *ACS Appl. Mater. Interfaces* **2016**, *8* (40), 27107–27114.

(67) Lokhande, V.; Lokhande, A.; Namkoong, G.; Kim, J. H.; Ji, T. Charge Storage in WO_3 Polymorphs and Their Application as Supercapacitor Electrode Material. *Results Phys.*

2019, *12* , 2012–2020.

(68) Zhu, M.; Meng, W.; Huang, Y.; Huang, Y.; Zhi, C. Proton-Insertion-Enhanced Pseudocapacitance Based on the Assembly Structure of Tungsten Oxide. *ACS Appl. Mater. Interfaces* **2014**, 6 (21), 18901–18910.

(69) B., B.; Cho, I.-H.; Bak, J.-S.; Kim, H.-J. V_2O_5 Nanorod Electrode Material for Enhanced Electrochemical Properties by a Facile Hydrothermal Method for Supercapacitor Applications. *New J. Chem.* **2018**, *42* (14), 11862–11868.

(70) Liu, X.; Sheng, G.; Zhong, M.; Zhou, X. Hybrid Nanowires and Nanoparticles of WO_3 in a Carbon Aerogel for Supercapacitor Applications. *Nanoscale* **2018**, *10* (9), 4209–4217.

(71) Nayak, A. K.; Das, A. K.; Pradhan, D. High Performance Solid-State Asymmetric Supercapacitor Using Green Synthesized Graphene-WO_3 Nanowires Nanocomposite. *ACS Sustain. Chem. Eng.* **2017**, *5* (11), 10128–10138.

(72) Huang, X.; Liu, H.; Zhang, X.; Jiang, H. High Performance All-Solid-State Flexible Micro-Pseudocapacitor Based on Hierarchically Nanostructured Tungsten Trioxide Composite. *ACS Appl. Mater. Interfaces* **2015**, *7* (50), 27845–27852.

(73) Jin, L. N.; Liu, P.; Jin, C.; Zhang, J. N.; Bian, S. W. Porous WO_3 /Graphene/Polyester Textile Electrode Materials with Enhanced Electrochemical Performance for Flexible Solid-State Supercapacitors. *J. Colloid Interface Sci.* **2018**, *510*, 1–11.

(74) Tian, Y.; Cong, S.; Su, W.; Chen, H.; Li, Q.; Geng, F.; Zhao, Z. Synergy of $W_{18}O_{49}$ and Polyaniline for Smart Supercapacitor Electrode Integrated with Energy Level Indicating Functionality. *Nano Lett.* **2014**, *14* (4), 2150–2156.

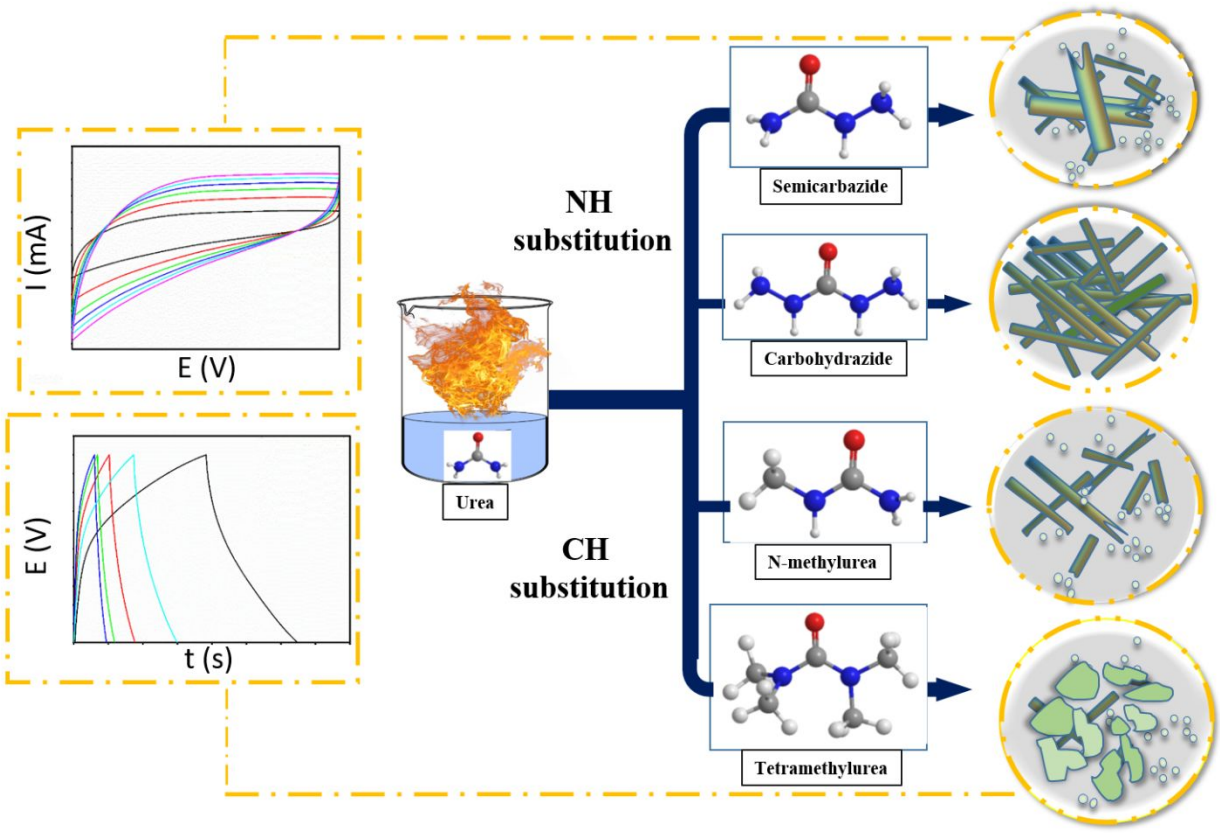
I (mA)
E (V)
E (V)
t (s)
Urea
NH
substitution
CH
substitution
Semicarbazide
Carbohydrazide
N-methylurea
Tetramethylurea

TOC Graphic